scientific reports

OPEN

A machine learning optimized Dielectric Ultra-focused Oscillatory (DUO) electrode for low temperature electrosurgery

Bo H. Choi[1], Jun H. Heo[2], Min S. Kim[2], In S. Choi[1] & Eun S. Lee[2]✉

The widespread adoption of radio frequency (RF) energy has made electrosurgery a cornerstone of modern surgical procedures, primarily due to its ability to minimize blood loss during, or independent of, tissue incision. Among the various electrosurgical modalities, monopolar electrodes have become indispensable in open surgeries and have been the focus of extensive research—exploring aspects such as electrode shape, material, surface coating, RF generator modulation, and feedback mechanisms involving temperature and impedance sensing. While electrosurgery delivers thermal energy for tissue cutting and coagulation, thermal effects represent both its principal utility and its greatest risk. Conventional monopolar electrodes operate at high temperatures (exceeding 250 ℃) to achieve surgical efficacy, but such conditions often result in substantial thermal damage to surrounding tissue and implanted devices. In response to these challenges, we propose a novel blade-type monopolar electrode employing dielectric heating as the primary energy delivery method. Unlike conventional electrodes, which generate heat via ohmic loss at the electrode–tissue interface, the proposed Dielectric Ultra-Focused Oscillatory (DUO) blade directly heats tissue moisture through focused dielectric energy, effectively eliminating surface heating of the electrode. This mechanism naturally restricts the maximum temperature to 100 ℃, governed by the phase transition of water vaporization. Experimental validation of the DUO blade demonstrated superior performance across key surgical metrics, including reduced operating temperature, shallower thermal necrosis depth, minimized blood loss, and decreased surgical smoke. These results underscore the DUO blade's potential to enhance surgical precision, safety, and visibility in electrosurgical applications.

Since 1926, when William Bovie, PhD—a professor of electrical engineering at the Massachusetts Institute of Technology—introduced the use of high-frequency radiofrequency (RF) energy for tissue cutting and coagulation, monopolar electrosurgery has become a widely accepted modality in modern surgical practice[1]. Both cutting and coagulation require the application of external thermal energy. This energy vaporizes or desiccates the water content in tissue, forming the fundamental basis for cutting and coagulation, respectively. Human tissue is generally classified as either high-water-content (> 50%) or low-water-content (< 50%)[2]. In RF electrosurgery, high-voltage waveforms generated by the electrosurgical unit (ESU) are delivered to biological tissue via monopolar or bipolar electrode systems, as illustrated in Fig. 1, to achieve cutting or coagulation effects through thermal energy. A critical consideration is determining the appropriate temperature range for surgical functionality. When a high-potential electrode with a small contact area interacts with relatively low-potential tissue, several physical phenomena can occur, including dielectric breakdown, dielectric heating, and conductive heating. Notably, momentary sparks caused by dielectric breakdown can generate localized temperatures exceeding several hundred degrees Celsius before full electrode–tissue contact is established. However, disregarding this transient phenomenon, the main objective remains reaching 100 °C, the boiling point of water at atmospheric pressure[3–5]. At this temperature, water undergoes phase transition, causing explosive vaporization and volumetric expansion that ruptures tissue, thereby facilitating cutting. In contrast, sub-boiling temperatures in the range of 60–80 °C cause denaturation and intracellular dehydration, promoting coagulation. This makes thermal modulation a key strategy for achieving hemostasis. Consequently, controlling electrode temperature has become central to technological advancements in RF electrosurgery.

[1]R&D division, CRESEN, Inc, Pleasanton, CA 94588, USA. [2]School of Electrical Engineering, Hanyang University ERICA Campus, Ansan 15588, South Korea. ✉email: eunsoo86@hanyang.ac.kr

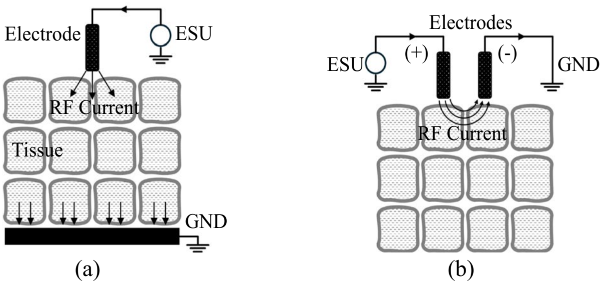

Fig. 1. RF electrosurgical systems: (**a**) Monopolar, (**b**) Bipolar.

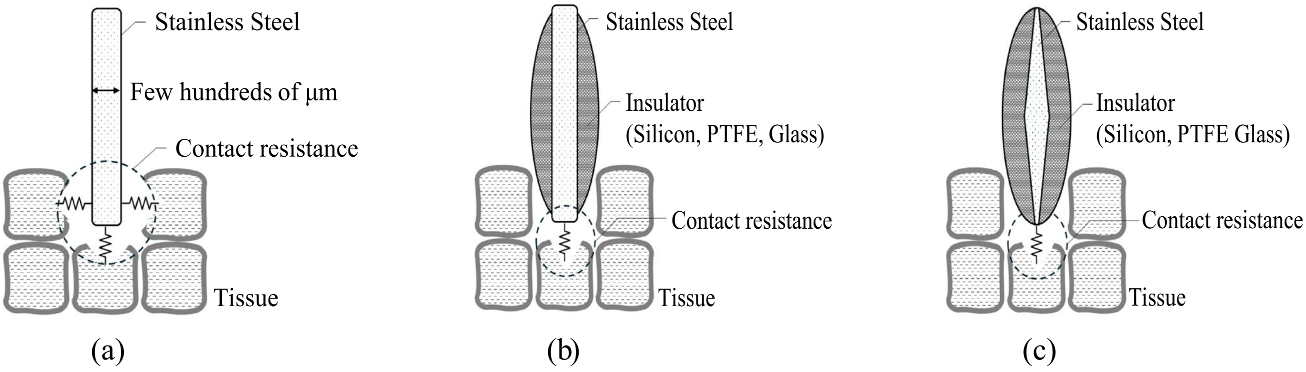

Fig. 2. Conventional monopolar electrode structure (front-view): (**a**) Uncoated blade-type electrode, (**b**) Coated blade-type electrode, and (**c**) Coated tapered blade-type electrode.

In this context, bipolar devices—which contain both active and return electrodes in a single unit—enable localized heating via a closed circuit. Meanwhile, monopolar devices, though widely used, have experienced a slower and less precise evolution in energy delivery control. The first RF monopolar electrode, commonly referred to as the Bovie or uncoated blade-type electrode, consisted of a thin stainless steel plate, as illustrated in Fig. 2(a). During use, it generates high-frequency current paths through adjacent tissue, with ohmic losses occurring at the electrode–tissue interface. These losses, dependent on contact resistance and current squared, produce localized heating directly surrounding the electrode, which then propagates to surrounding tissues, causing destruction and coagulation. While this conductive heating mechanism is intuitive and offers rapid surgical response, it has drawn criticism for producing excessive heat (often exceeding 250 °C) at both the electrode and the tissue interface[3]. This can result in thermal damage that negatively affects wound healing and cosmetic outcomes[6,7]. At temperatures above 200 °C, organic molecules degrade via carbonization, leaving black or brown residues—a phenomenon known as black coagulation. Moreover, elevated electrode temperatures pose a significant threat in surgeries involving implanted medical devices. In particular, in the field of electrophysiology—where hundreds of thousands of procedures are performed annually in the United States alone—there have been multiple reports highlighting the risk of thermal damage to insulation materials on components such as pacing leads. These findings emphasize the potential hazard of high-temperature electrodes in device-dependent surgical interventions[8,9].

In addition to these direct effects, high-temperature electrodes can also lead to secondary harmful consequences for the overall surgical environment, most notably the generation of surgical smoke. In addition, surgical smoke—an unavoidable byproduct of electrosurgery—is known to contain a significant amount of hazardous chemical and biochemical compounds[10–17]. It consists primarily of submicron-sized particles that are not effectively blocked by standard surgical masks[18,19]. Excessive electrode temperatures are widely recognized to exponentially increase both the quantity and toxicity of surgical smoke. In response to the associated health risks for medical personnel, more than 15 U.S. states have enacted legislation mandating the evacuation or reduction of surgical smoke in operating rooms[20]. This has led to a growing demand not merely for smoke evacuation systems, but for fundamental technological solutions capable of minimizing smoke generation at its source[21–23].

As illustrated in Fig. 2(b), to mitigate the thermal damage described above, coated blade-type electrodes have been developed by incorporating insulating materials such as silicone, Teflon (PTFE), or glass along the lateral surfaces of the electrode. While these coatings help block heat transfer in specific directions, they fail to address the underlying issue: the fundamental energy transfer mechanism. Consequently, the uninsulated electrode edge remains a hotspot for excessive heat, leaving the risk of thermal damage largely unresolved. Subsequently, an advanced version of the coated electrode was introduced, featuring a tapered geometry with an electrically uninsulated edge, as illustrated in Fig. 2(c). This design was intended to drastically reduce the electrode–tissue contact area, thereby enabling the localized application of reduced thermal energy; to simultaneously achieve the tapered geometry, mechanical stiffness, and reduced friction with tissue during incision, an elliptical contour was often adopted from the central shaft to the tapered edge[24]. Beyond structural enhancements to the electrode, efforts have also focused on modulating the output waveform of the electrosurgical unit (ESU), which typically delivers high-frequency alternating voltage exceeding several hundred kilohertz, often modulated at sub-kilohertz frequencies. A pulse-modulated RF voltage was applied to the tapered electrode with a sharp, glass-coated edge, enabling effective tissue incision at substantially reduced temperatures compared to conventional electrosurgical tools[25–27]. The application of an insulated, tapered electrode designed to minimize resistive heating—together with pulse-modulated RF power to maximize dielectric breakdown and plasma-induced heating—has enabled cutting at significantly lower temperatures. However, this temperature reduction compromises the ability to coagulate nearby blood vessels during incision. As a result, studies have reported higher intraoperative blood loss relative to that observed with conventional electrosurgical systems[6].

This paper provides a detailed analysis of the energy transfer mechanisms in monopolar RF electrosurgery and introduces a novel technology—the Dielectric Ultra-Focused Oscillatory (DUO) electrode—designed to minimize thermal damage, reduce blood loss, and suppress surgical smoke through dielectric heating. The proposed DUO electrode was optimally designed in a blade-type configuration using electric field simulations based on finite element analysis (FEA) integrated with machine learning. It was further engineered to operate without the need for additional RF modulation.

The proposed DUO blade, a blade-type DUO electrode, was experimentally evaluated against three conventional combinations of monopolar electrodes and ESUs commonly used in clinical settings. The results demonstrated its superiority in terms of reduced operating temperature, minimized thermal damage to surrounding tissue, decreased blood loss, and significantly lower levels of surgical smoke. To evaluate the operating temperature, ex-vivo tests were conducted using chicken breast tissue. For the assessment of tissue damage, bleeding, and surgical smoke, full-thickness incision tests were performed on healthy 8-month-old Yucatan pigs. The animal study was conducted in accordance with Korean IACUC guidelines, with prior approval, at a certified and authorized animal research facility.

The proposed energy transfer mechanism and electrode design

Mechanisms of energy transfer in RF electrosurgery for thermal interaction with biological tissue

RF electrosurgery achieves tissue heating by delivering high-frequency electrical energy, typically in the range of hundreds of kilohertz to several megahertz. For surgical applications such as cutting and coagulation, frequencies in the hundreds of kilohertz are most commonly used. The system consists of an RF generator (ESU) and electrodes that establish electrical potential across tissue. RF electrodes are generally classified as monopolar or bipolar, depending on the configuration controlled by the surgeon. In bipolar systems, current flows across a confined tissue path between two electrodes. In contrast, monopolar systems deliver RF energy along a broader path, as depicted in Fig. 1[28], with the active electrode in contact with the tissue and the return path completed via patient grounding. As shown in Fig. 2, the monopolar electrode—constructed from conductive metal and insulating materials—delivers high-voltage RF energy from the ESU to the tissue. This energy transfer gives rise to three distinct heating mechanisms: dielectric heating through oscillating electric fields, resistive heating from conduction currents, and localized heating associated with electron avalanche effects.

Dielectric heating in RF electrosurgery occurs when polar molecules—primarily water—respond to high-frequency alternating electric fields by oscillating, generating heat through friction. As water is the primary constituent of human tissue, the polarity of water molecules (H_2O), due to differences in electron affinity between hydrogen and oxygen, makes them highly responsive to these fields. Oscillating at rates over 400,000 times per second, water molecules collide with adjacent molecules, increasing thermal motion and producing heat. This selective heating of intracellular moisture induces a temperature rise within the tissue itself rather than at the electrode–tissue interface. Moreover, the temperature elevation is inherently self-limiting due to the vaporization threshold of water at 100 °C, which prevents excessive thermal buildup. As a result, this mechanism is considered both safe and effective for cutting and coagulation, with minimized collateral damage. The amount of heat generated W is influenced by the tissue's relative permittivity ε), dielectric loss tan δ, electric field intensity E, and frequency f, as in Eq. (1)[29,30].

$$W \propto \varepsilon_r \cdot tan\delta \cdot f \cdot E^2 \left[W/m^3\right] \tag{1}$$

Effective dielectric heating under fixed frequency and voltage conditions requires precise optimization of electrode shape and insulation in order to intensify the local electric field. This has long presented a critical challenge in the design of monopolar electrosurgical electrodes. Ensuring that the electrode retains a high potential during contact with low-potential tissue demands the use of advanced materials and engineering approaches. These include the development of high-durability conductors and insulators, along with detailed analysis and modeling to ensure stability under high-voltage, high-temperature operating conditions.

For the reasons outlined above, the vast majority of monopolar electrodes rely on resistive heating—commonly described by the I^2R or V^2/R principle—to generate thermal energy in tissue. The critical factor in this mechanism is the resistance R, which is primarily governed by the contact resistance between the conductive electrode and the tissue surface. This is particularly important because the cross-sectional area of the RF current path increases significantly as current travels from the electrode–tissue interface to the patient's grounding pad. Resistance values typically range from several hundred to several thousand ohms and vary depending on factors such as surface roughness of both the tissue and electrode, as well as tissue moisture content. Therefore, the amount of heat generated via resistive heating is determined by the total impedance of the RF path, which includes this surface-level contact resistance.

In addition to the two primary heating mechanisms described above, most monopolar electrodes are also subject to an unavoidable phenomenon known as dielectric discharging. Regardless of the heating principle employed, electrodes designed for efficient cutting typically feature thin, narrow (blade-shaped) or sharp, pointed (needle-shaped) designs. These shapes often result in dielectric breakdown of the air—or, in surgical environments, air mixed with blood and other impurities—just before making physical contact with the low-potential tissue. These air dielectric breakdown events, which occur over extremely short durations (on the microsecond level), are highly localized and random, making them almost impossible to intentionally control by the user. They have traditionally been considered an unavoidable phenomenon during RF surgery. However, certain electrosurgical unit (ESU) modes, such as those employing high-voltage pulsed waveforms, are sometimes used to intentionally increase the frequency of these breakdown events[31]. The accompanying electron avalanche phenomenon, which occurs simultaneously with dielectric breakdown, can cause the tissue temperature at the discharge point to rise instantaneously to several hundred to over a thousand degrees Celsius. This results in immediate tissue destruction (e.g., rupture and carbonization) and provides an associated hemostatic effect at the site.

Monopolar blade-type electrode structure for efficient dielectric heating

From bare metal to laterally insulated designs, conventional monopolar blade-type electrodes have been developed to minimize collateral thermal damage by limiting tissue contact to the cutting edge during electrosurgery. Further refinement led to the Advanced Energy Blade, incorporating a sharpened tip and advanced coatings such as glass or composite anti-adhesive materials. While this design improves precision and reduces tissue injury compared to silicone- or Teflon-coated predecessors, it still operates using conventional resistive heating. As a result, high temperatures along the blade and incision site continue to pose risks of thermal damage to surrounding tissues and implanted devices.

Figure 3 illustrates the proposed DUO monopolar blade electrode, as first introduced by the authors[32,33] in Fig. 3(a) and (b), which is optimized for capacitive coupling–based dielectric heating with adjacent tissue to enhance the safety and precision of RF electrosurgery. The design aims to reduce collateral tissue damage, protect implanted devices, and minimize thermal necrosis and carbonization. As illustrated in Fig. 3(c), the proposed electrode is designed to utilize dielectric heating as the primary energy transfer mechanism for tissue dissection. The electric field emitted from the electrode selectively heats water molecules within the tissue, and this localized heating results in tissue coagulation caused by thermal denaturation, as well as cellular rupture due to vaporization-driven cutting. Once the water content in the targeted region is depleted due to vaporization, further heating naturally ceases. This built-in temperature-limiting behavior serves as a key design principle, enabling controlled and safe energy delivery during electrosurgery. The tapered geometry of the electrode, narrowing from the center toward the edge, was designed to work in conjunction with the insulated edge to enhance electric field concentration at the tip and to maximize the frequency of secondary dielectric breakdown and the resulting plasma discharges at the tissue–electrode interface. This secondary dielectric breakdown mechanism, though relatively weak in magnitude, provides a directional and supplemental pathway for energy

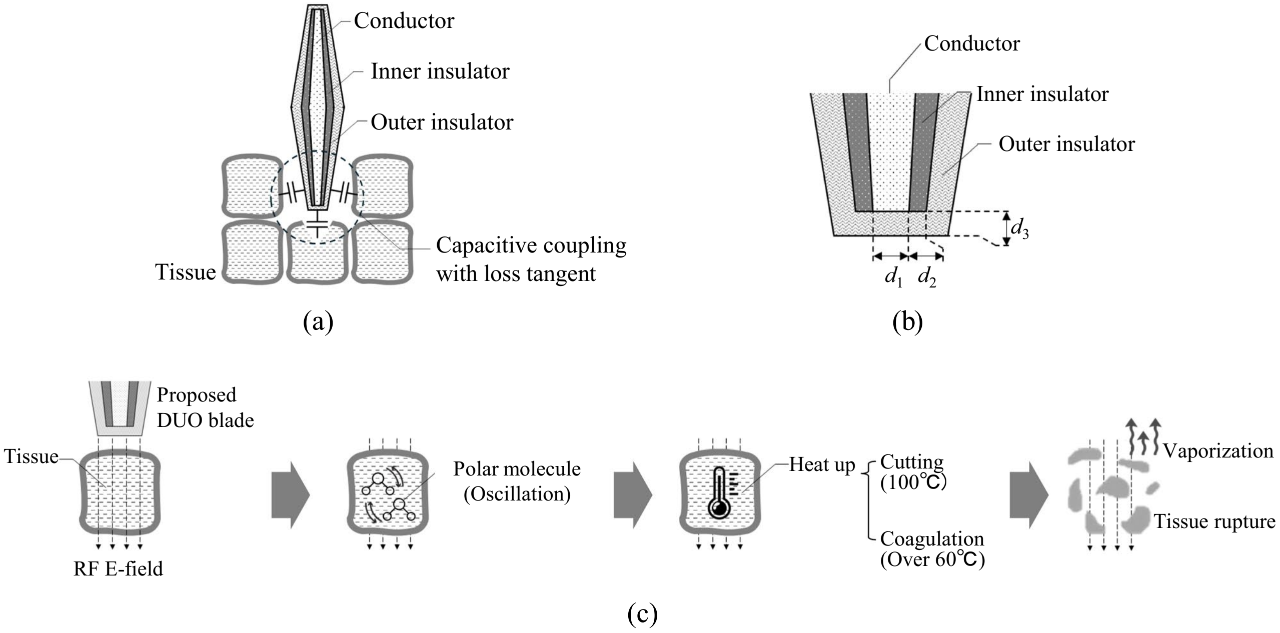

Fig. 3. Proposed dielectric ultra-focused oscillatory (DUO) blade for electrosurgery: (**a**) Structure and the concept of capacitive coupling with tissue, (**b**) Blade edge and its key design variables, (**c**) Heating mechanism.

Parameters	Relative Permittivity	Bulk Conductivity (S/m)
aluminum	1	3.8e+7
metal oxide	9.8	1e-12
PFTE	2.1	1e-7
Liver	3288.8	1.3e-1
Dried tissue	10	1e-1

Table 1. Material properties used in the blade design.

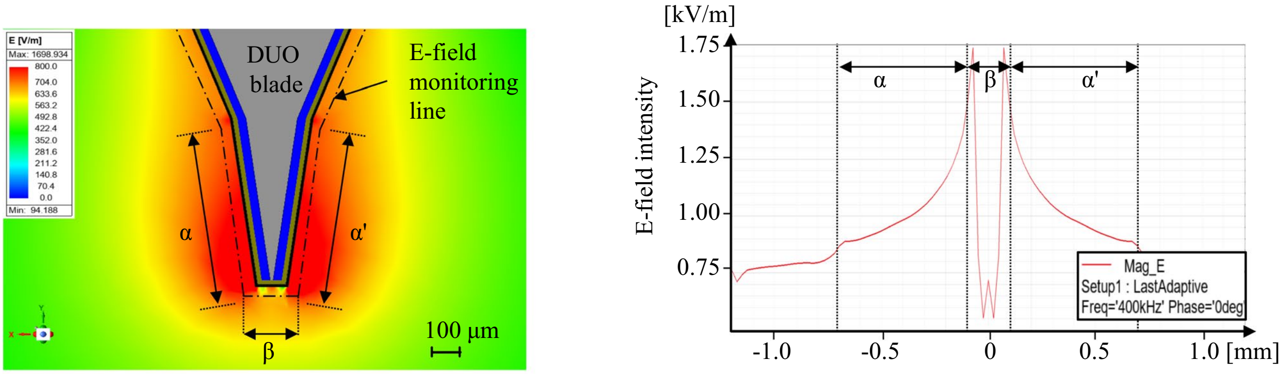

(a) E-field distribution

(b) E-field intensity profile 50 μm apart to the blade surface

Fig. 4. FEM analysis results result when 400 kHz 100 V sinusoidal voltage is applied for the proposed DUO blade.

delivery that facilitates tissue cutting. Simultaneously, the tapered shape helps to minimize mechanical friction between the electrode surface and the tissue during incision, contributing to smoother and more precise surgical performance.

To achieve the aforementioned design objectives, the blade incorporates a precisely sharpened edge and a laminated dual-insulation structure composed of a metal oxide layer and PTFE. The device is fabricated by forming an anodized aluminum oxide (Al_2O_3) layer on an aluminum core—chosen for its controllable oxide thickness—and subsequently applying a PTFE spray coating on the exterior. Each layer possesses a distinct dielectric constant, and these materials are strategically arranged to concentrate the electric field at the cutting edge while simultaneously supporting hemostasis along the lateral surfaces. The thicknesses of both the blade tip and insulating layers were optimized through finite element analysis (FEA) and validated experimentally, confirming the superior thermal performance of the DUO electrode.

Optimization of electrode structure using finite element analysis and deep reinforcement learning

The structure of the proposed DUO blade was optimized to adjust the electric field distribution at a distance of 50 μm from the electrode, which is greater than the average diameter of tissue structures encountered in electrosurgery[34]. To achieve an appropriate balance between cutting and coagulation effects by tailoring the electric field, a deep reinforcement learning (DRL) framework integrated with finite element analysis (FEA) was employed to identify the optimal solution among a wide range of candidates[35]. Considering the characteristic of dielectric heating being proportional to the square of the electric field as described in Eq. (1), the optimal thicknesses of each layer—d_1, d_2, and d_3 in Fig. 3—and their combination were defined as design goals to ensure that the integrated electric field in the vertical direction (normal to the blade–tissue interface) is 30% greater than that in the horizontal direction. The DRL agent observes the current design state as a vector consisting of three thickness parameters. The electromagnetic simulation was conducted using the dielectric and conductive properties of the materials listed in Table 1[36]. Liver tissue was selected as the bulk material for evaluation, as it is a representative soft, high–water-content tissue containing a dense vascular network, and thus exhibits electrical conductivity and permittivity characteristics representative of various biological tissues. To simulate the presence of inevitable necrotic tissue during electrosurgery, a 5 μm-thick layer of dry tissue was assumed to surround the blade in the analysis model. Each layer in Fig. 3(a) was selected based on their distinct electrical and thermal properties, with aluminum serving as a conductive core, metal oxide as a high-permittivity dielectric, and PTFE as an insulator with anti-adhesive characteristics as in Table 1. The averaged integrated electric field intensities between intervals of α and β in Fig. 4 were monitored, and various combinations of the critical design variables were explored and optimized using the proposed deep reinforcement learning framework, as illustrated in Fig. 5.

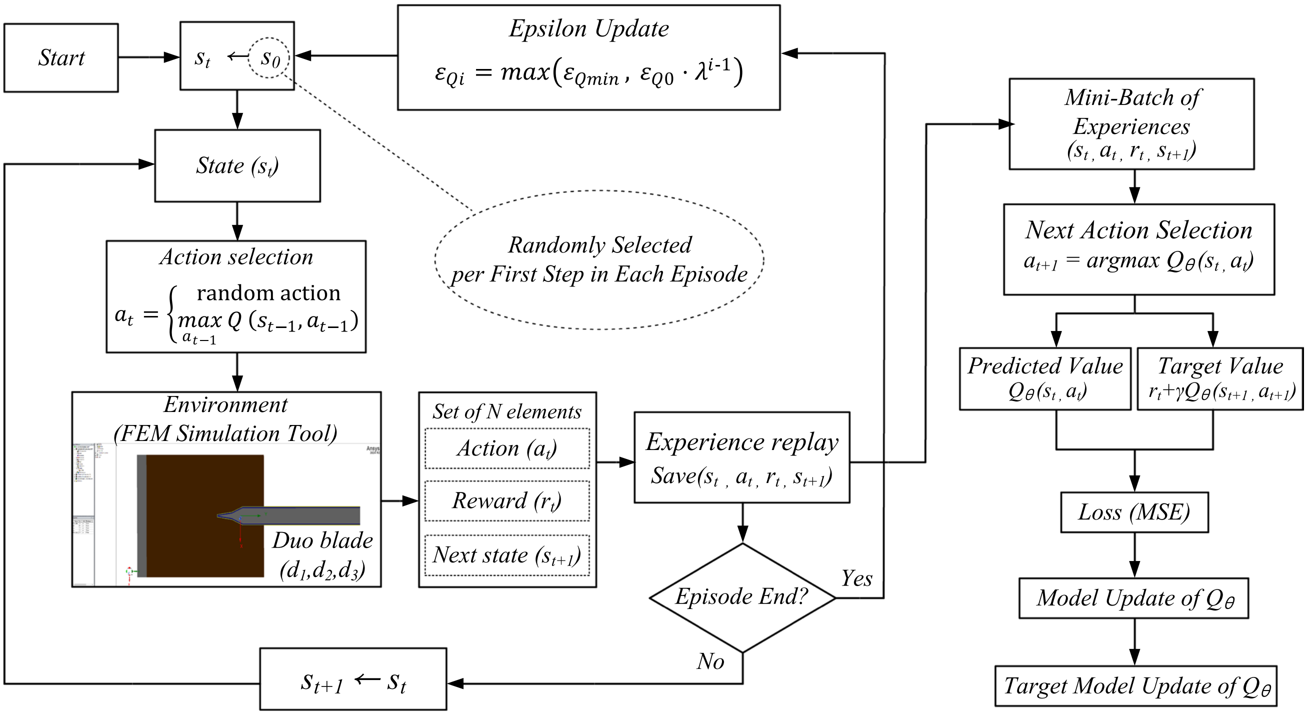

Fig. 5. Operational mechanism of the proposed DRL algorithms.

Category	Parameter	Description	Value
Q-learning	discount factor (γ)	Discount rate for Q-value (reward) of future values ($0 \le \gamma \le 1$)	0.85
	learning rate (α)	The proportion of new learning results reflected ($0 \le \alpha \le 1$)	0.001
	epsilon (ε_Q)	The ratio of exploring various actions, decreasing from the initial value to the final value	1.0 → 0.2
	epsilon decay (λ)	Gradual reduction of the exploration rate over time to stable learning	0.99
	Target network update	Frequency of updating the target network with episodes	1
Experience replay	batch size	Amount of data used for learning at once	64
	memory size	Size of the memory that stores learning data	2000
Network configuration	Input layer	Number of input nodes, i.e., state variables	3
	Hidden layer	Number of nodes in the hidden layer, adjusting the complexity of the model	32-32
	Output layer	Number of selectable actions	7
	Loss	Loss function, Mean Squared Error (MSE)	
	Optimizer	Optimization algorithm, Adam	

Table 2. Hyperparameter selection for the proposed deep reinforcement learning.

The optimization was guided by a Deep Q-Network (DQN) algorithm[37]. Each combination of (d_1, d_2, d_3) represented a state, and possible actions included increasing, decreasing, or maintaining each parameter. Learning proceeded over episodes consisting of 50 steps, following an ε-greedy policy[38]. Initially, the agent fully explored the action space (ε_Q=1.0) and gradually shifted toward exploitation as ε_Q decayed with each episode. The overall structure of the proposed DRL-based optimization procedure is illustrated in Fig. 5, and the appropriate hyperparameters for the proposed DRL is summarized in Table 2[3940]. These hyperparameters were selected to ensure a stable learning process and efficient convergence. The discount factor γ balances immediate and future rewards, while a small learning rate α provides gradual updates to avoid oscillations. An exponentially decaying exploration rate λ enables a smooth transition from exploration to exploitation. The replay buffer size and batch size were chosen to ensure training stability and sufficient sample diversity. The network architecture (3-32-32-7) reflects the dimensionality of the state and action spaces and provides sufficient capacity for policy approximation. The DRL agent observes the current design state as a vector consisting of three thickness parameters as shown in Eq. (2):

$$s_t = \begin{bmatrix} d_1(t) \\ d_2(t) \\ d_3(t) \end{bmatrix} \tag{2}$$

Modifying multiple design parameters simultaneously leads to an exponential increase in the design space, which destabilizes the training process. Accordingly, the action space $a_t \in R^3$ is constrained such that only one component is modified, or all components remain unchanged at each step. Thus, at every step, either one of the parameters d_1, d_2, or d_3 is adjusted by ± Δ or no change occurs. This results in a total of 7 possible discrete actions, as in Eqs. (3) and (4).

$$\mathcal{A} = \left\{ \begin{bmatrix} \pm 5 \\ 0 \\ 0 \end{bmatrix}, \begin{bmatrix} 0 \\ \pm 10 \\ 0 \end{bmatrix}, \begin{bmatrix} 0 \\ 0 \\ \pm 5 \end{bmatrix}, \begin{bmatrix} 0 \\ 0 \\ 0 \end{bmatrix} \right\} \tag{3}$$

.

$$s_{t+1} = s_t + \Delta\, a_t\,, \quad where\; a_t \in \mathcal{A} \tag{4}$$

After each action, the FEA simulation yielded an updated electric field distribution. A scalar reward was then computed based on how closely this distribution aligned with a predefined optimal energy pattern between the blade's edge and side regions, as illustrated in Fig. 4(b). The reward formulation is given in Eq. (5) which evaluates how effectively the electric field remains within a desired intensity range across the specified region.

$$R(d_1, d_2, d_3) = \frac{1}{x_{max} - x_{min}} \int_{x_{min}}^{x_{max}} I\left(E_{min} \le E(x) \le E_{max}\right) dx \tag{5}$$

The experiences were stored in a replay buffer and used for mini-batch training of the Q-network. The Q-values were updated using the Bellman Eq. 3[8] which defines the target value y_t for each state-action pair as in Eq. (5), where each episode $i \ge 1$ consisted of 50 simulation steps $t \in \{1,2,\ldots,50\}$.

$$y_t = r_t + \gamma \max_{a_{t+1}} Q_{\theta^-}(s_{t+1}, a_{t+1}) \tag{5}$$

In Eq. (5), $\gamma \in [0,1]$ is the discount factor, Q_θ^- is the target Q-network with parameters θ^-, and s_{t+1}, a_{t+1} are the next state and action, respectively. The loss function was defined as the mean squared error between the predicted and target Q-values, and the network weights were optimized using gradient descent. The loss is computed as in Eq. (7)[3738].

$$\mathcal{L}(\theta) = E_{(s_t, a_t, r_t, s_{t+1})}\left[\left(y_t - Q_\theta(s_t, a_t)\right)^2\right] \tag{6}$$

To ensure stability, the target network was periodically synchronized with the main Q-network, allowing the agent to gradually converge to an optimal combination of structural thicknesses through the iterative learning process. The progression of this process is illustrated in Fig. 6, which presents representative results from episodes 1 and 200, showing the evolution of action selection and parameter tuning, while the intermediate results from episodes 30 and 120, demonstrating gradual convergence, are provided in Supplementary Fig. S1. In each episode, the agent selected an action from a discrete space consisting of increase, decrease, or maintain operations for each design parameter d_1, d_2, and d_3. The top panels of Fig. 6 show the probability distribution for each action, while the bottom panels show the corresponding parameter values and the resulting electric field ratio between the edge and side. The action selection policy follows an ε-greedy rule as in Eq. (7).

$$a_t = \begin{cases} \text{random action} & \text{with probability}\,\epsilon_{Qi} \\ \underset{a}{argmax} Q(s_t, a) & \text{with probability } 1 - \epsilon_{Qi} \end{cases} \tag{7}$$

The ε-value decays over time, as in Eq. (8), ensuring a gradual transition from exploration to exploitation by exponentially reducing the exploration rate until it reaches a predefined minimum threshold ϵ_{Qmin}.

$$\epsilon_{Qi} = \max\left(\epsilon_{Qmin},\ \epsilon_{Q0} \cdot \lambda^{i-1}\right) \tag{8}$$

Initially, in episode 1, the exploration rate ε_{Q0} in Eq. (8) was set to 1.0, resulting in fully random behavior. As training progressed and ε_Q decayed, the agent increasingly favored high-reward actions. By episode 30, exploitation behavior had begun to dominate. Episode 120 marked a transitional phase where the agent refined its selections, and by episode 200, the electric field distribution progressively aligned with the desired energy localization pattern, confirming the agent's ability to converge toward an optimal design. The corresponding optimal layer thicknesses were determined to be 10 µm for d_1, 30 µm for d_2, and 20 µm for d_3. The final design achieved an electric field ratio of 1.305 between the blade edge β and lateral surface α, corresponding to the highest reward observed during training, thereby verifying the efficacy of the DRL-guided optimization process.

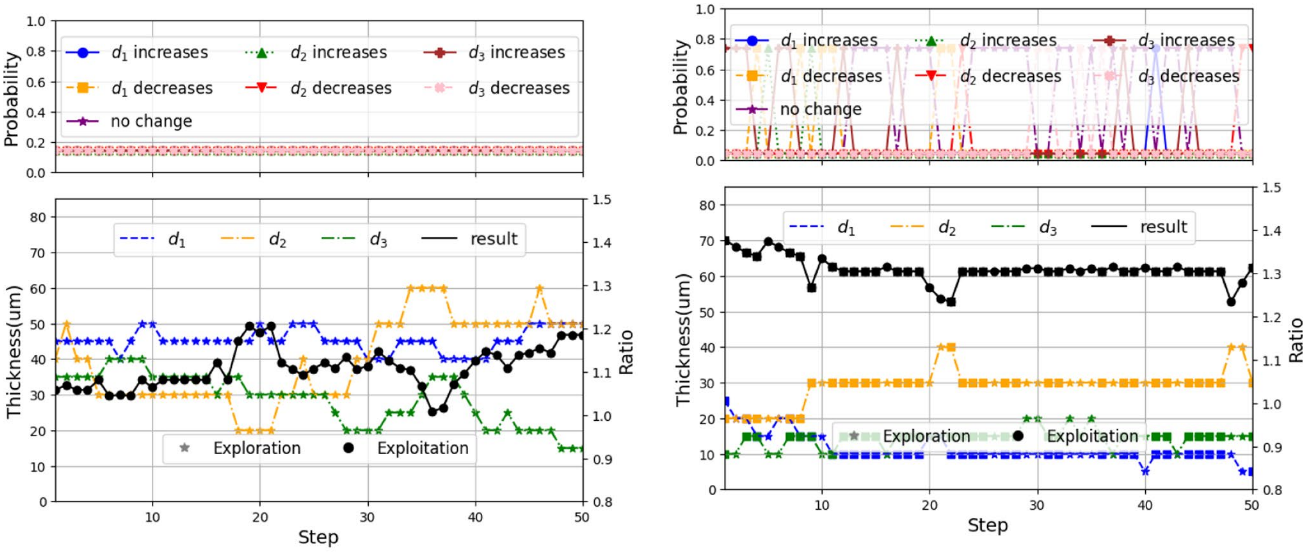

(a)

(b)

Fig. 6. Progression of the proposed DRL: (**a**) Episode 1: initial exploration phase, (**b**) Episode 200: Convergence to optimal design parameters.

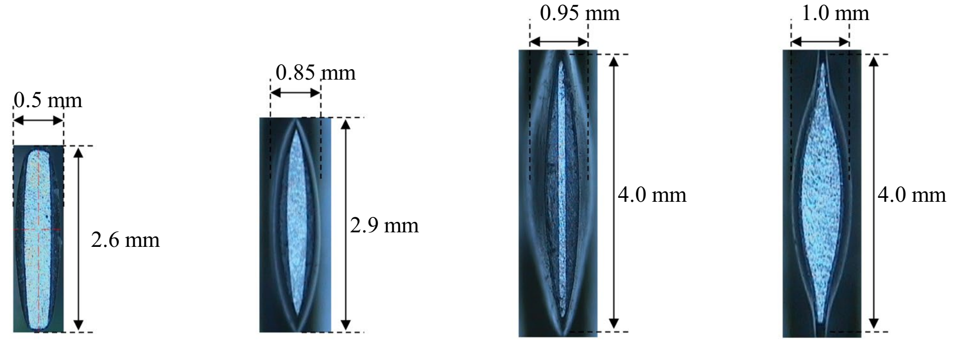

(a)

(b)

(c)

(d)

Fig. 7. Electrodes used for experimental verification: (**a**) Coated blade, (**b**) Coated and tapered blade -A, (**c**) Coated and tapered blade -B, and (**d**) Proposed DUO blade.

Experimental verification

The proposed DUO blade was fabricated based on the optimal design parameters described in the previous section, as illustrated in Fig. 7, and its performance was evaluated through both ex-vivo and in-vivo experiments. All ex-vivo and in-vivo experiments were conducted at room temperature (25 ℃) and humidity (30~50%) to simulate real surgical conditions. To assess its effectiveness, comparative tests were conducted against three commercially available monopolar blade-type electrodes (Supplementary Fig. S2): Valleylab Edge Blade Electrode (coated blade), Medtronic PlasmaBlade (coated and tapered blade-A), and Stryker PhotonBlade (coated and tapered blade-B). The comparative electrodes were selected from representative commercial monopolar blade-type devices, considering key factors such as the presence of a tapered geometry, and the type and thickness of the insulation material, including silicone and glass. Fig. 7 shows the cross-sectional views of the proposed DUO blade and the comparative commercial blades, measured using a video measuring system (VMS-2010G, Rational). In the cross-sectional images, the conductive metal region appears as a light gray area, while the applied insulation layers are distinguishable as dark gray regions. The insulation structure, measured dimensions, and material composition of each electrode are summarized in Table 3. Although the vertical length of each electrode cross-section varies from 2.6 mm to 4 mm, as shown in Fig. 5, this factor is not directly related to the thermal effects, which are the primary focus of this study. Therefore, the experimental devices were selected based on the horizontal cross-sectional length, including the thicknesses of both the conductive metal and insulation layers. For each device, if a specific RF generator was required for operation, the corresponding generator recommended by the manufacturer was used to ensure compatibility and optimal performance. The experimental devices selected according to the criteria described above are listed in Table 4. A scalpel was additionally included to

Device	Insulation Structure	Material			Thickness [mm]		
		Base metal	1st insulation	2nd insulation	Metal (edge)	1st insulation	2nd insulation
Coated blade	Monolayer	Stainless Steel	Silicon	-	0.35	0.11	-
Coated and tapered blade -A	Monolayer	Stainless Steel	Glass	-	0.01	0.17	-
Coated and tapered blade -B	Bilayer	Stainless Steel	Glass	Teflon	0.01	0.17	0.08
Proposed DUO blade	Bilayer	Aluminum	Aluminum Oxide	Teflon	0.01	0.03	0.02

Table 3. Structural analysis of electrodes.

Device	Heating Energy	Generator	Waveform	Frequency [kHz]	Power [W]	Open Circuit Voltage [V_{rms}]	Experimental Case
Scalpel (No. 10)	None	None	None	None	None	None	G1
Coated blade	Resistive	X	Continuous, Sinusoidal	390	35 W	320	G2-L
					50 W	420	G2-H
Coated and tapered blade -A	Resistive	X	Continuous, Sinusoidal	390	35 W	320	G3-L
					50 W	420	G3-H
Coated and tapered blade -B	Resistive	Y	Continuous, Sinusoidal	469	35 W	156	G4-L
					50 W	156	G4-H
Proposed DUO blade	Dielectric	X	Continuous, Sinusoidal	390	35 W	320	G5-L
					50 W	420	G5-H

Table 4. Experimental cases.

serve as a baseline control for the evaluation of intraoperative blood loss. As summarized in Table 4, two types of RF generators—Valleylab Force FX (X) and Medtronic AEX (Y)—were used in the experiments, each selected and configured according to the operational requirements of the corresponding electrosurgical electrodes. Although the two electrosurgical generators used in this study operate at different frequencies, the difference is relatively minor considering that the typical frequency range for electrosurgery spans from 100 kHz to several MHz. Additionally, the frequency differences were considered negligible in terms of tissue electrical properties, such as conductivity and permittivity[41,42], and were therefore unlikely to affect the experimental outcomes. The generators were operated in the cutting mode, which delivers a continuous sinusoidal waveform and enables consistent energy delivery, while low-power modes involving RF modulation and the coagulation mode were excluded to clearly isolate and evaluate the performance characteristics resulting from electrode design. Output power settings of 35 W and 50 W, which are most commonly used and recommended for general surgery, were applied as experimental conditions for each generator, in accordance with the manufacturer's published Instructions for Use (IFU)[43,44]. The authors fully acknowledge that the indicated power values on RF generators do not necessarily represent constant output power, but rather reflect a control scheme in which the generator maintains a constant voltage while limiting output based on the selected power setting. However, considering that the displayed power setting is the only adjustable parameter available to medical professionals during actual surgical procedures, the experiments were designed to use these values in order to closely simulate real-world clinical conditions. Accordingly, calibrated commercial RF generators were used, and the displayed power output was adopted as the reference standard for experimental design.

A total of four types of experiments were designed for this study. Except for the operating temperature measurement, all other evaluations—including tissue necrosis, blood loss, and surgical smoke—were conducted using a single 8-month-old Yucatan pig. These in-vivo tests were designed in compliance with the ARRIVE guidelines and conducted at K-MEDIhub, a certified animal research facility, following approval from the Institutional Animal Care and Use Committee (IACUC) in Korea and in accordance with national ethical regulations for animal experimentation. All devices used in the in-vivo experiments, including the proposed DUO blade, were FDA-approved commercial products deemed safe for use in both animals and humans. As illustrated in Fig. 8, six experimental zones were defined along the left and right sides of the pig's spine for in-vivo analysis. Each zone included a total of nine full-thickness incisions, consisting of one scalpel incision and eight electrosurgical incisions performed using four different devices, each tested at two output power levels. Each incision was designed to be 3 cm in length, with a 2 cm spacing between adjacent incisions, and the order and position of each incision were randomly assigned within each zone. All incisions were performed at a controlled speed of 1 cm per second using a precision stopwatch to ensure experimental consistency, and the procedures were carried out by a veterinary surgeon experienced in electrosurgical techniques.

Operating temperature

To observe the temperature of both the electrode and tissue during incision under each experimental condition, thermal imaging was conducted using a high-resolution infrared thermal imager (U5857, Keysight). 200 g samples of fresh chicken breast, adjusted to room temperature, were prepared to assess each test condition. The peak temperature at the cutting site was measured five times for each incision, and the average value was used

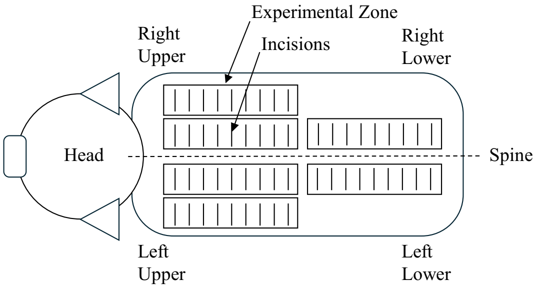

Fig. 8. Incision site allocation for in-vivo experiment.

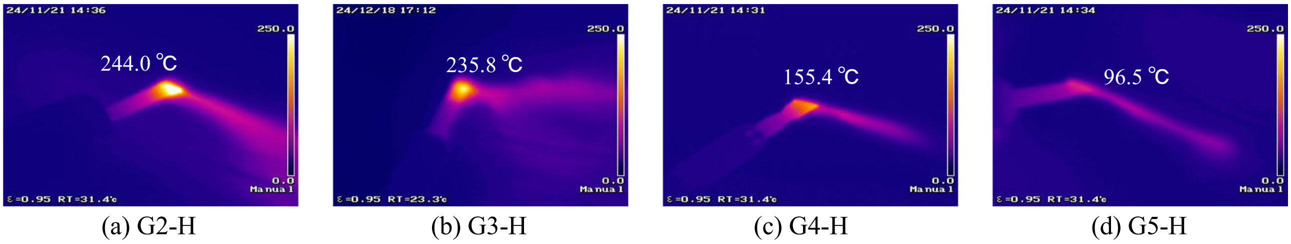

(a) G2-H (b) G3-H (c) G4-H (d) G5-H

Fig. 9. Thermal images captured during operating temperature experiments at 50 W and the corresponding average maximum temperatures.

for analysis, as in Supplementary Table S1. As shown in Fig. 9, there were significant differences in the peak temperatures observed at the incision sites under each experimental condition. Notably, the proposed DUO blade, which operates based on dielectric heating, exhibited a self-limiting thermal effect, with temperatures consistently remaining below 100 °C, unlike the other experimental groups. In both the 35 W and 50 W cases, the proposed DUO blade exhibited a lower operating temperature than other groups, with the temperature inherently limited to 100 °C, and the measurement results for the 35 W condition are presented in Supplementary Fig. S3. The combination of glass insulation and a tapered electrode geometry demonstrated improved thermal performance compared to conventional silicone-coated electrodes under identical RF power conditions. However, commercial devices based on resistive heating exhibited localized overheating, with temperatures exceeding 100 °C at the interface between the electrode and tissue, due to the concentration of current in the contact area.

Thermal injury

In electrosurgery, where incisions are made by applying high temperatures to biological tissue, the surrounding area is inevitably affected by thermal spread. Minimizing the extent of thermal necrosis has become a key focus in the advancement of modern electrosurgical technologies. Accordingly, quantitative assessment and comparison of necrosis were performed through histological analysis. From each full-thickness incision site, a central tissue region was biopsied using a 12 mm circular punch, extracting the full dermal thickness. The harvested samples were fixed in neutral buffered formalin, embedded in paraffin blocks, and sectioned into tissue slides. These slides were stained using Masson's trichrome and imaged using a digital microscope. Necrosis depth was measured at four points showing the greatest extent of damage on both the left and right sides of the incision line. All measurements were performed using the ImageJ software platform, with image analysis conducted through Fiji, an enhanced distribution of ImageJ.

Figure 10 presents representative histological images obtained under each experimental condition at the 50 W power setting, where yellow boxes indicate the measurement points for necrosis depth, while the corresponding histological images for the 35 W power setting are provided in Supplementary Fig. S4. The depth of thermal coagulation necrosis caused by each blade, extracted from these images, was quantitatively analyzed as shown in Fig. 11, with the average values for each group provided in Supplementary Table S2. This corresponds to the dark red regions extending laterally from the center of the incision and visually represents tissue necrosis including denatured collagen[6]. In the box-and-whiskers plot shown in Fig. 11, the box represents the range between the first and third quartiles, the horizontal line inside the box indicates the median value, and the whiskers show the entire range of data including the lowest and highest measurements. The average necrosis depths for each experimental condition were measured in the following order: G2-L (105 μm), G2-H (98.5 μm), G3-L (36.3 μm), G3-H (45.3 μm), G4-L (30.0 μm), G4-H (41.4 μm), G5-L (31.8 μm), and G5-H (38.5 μm). The measured necrosis depths followed the same trend as the previously recorded operating temperatures, with the proposed DUO blade (G4) showing a statistically significant reduction in necrosis depth compared to the non-tapered, uncoated blade (G2) ($P < 0.001$ at 35 W; $P = 0.005$ at 50 W). Higher incision temperatures were associated with increased tissue necrosis, which may potentially correlate with slower wound healing rates in

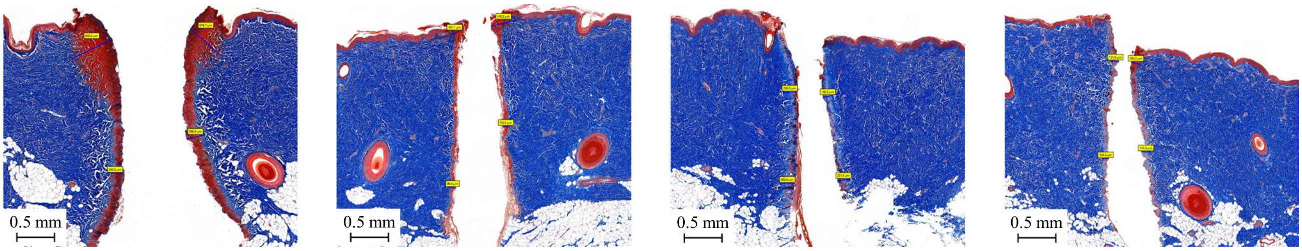

(a) G2-H (b) G3-H (c) G4-H (d) G5-H

Fig. 10. Representative histological images of each experimental case at the 50 W.

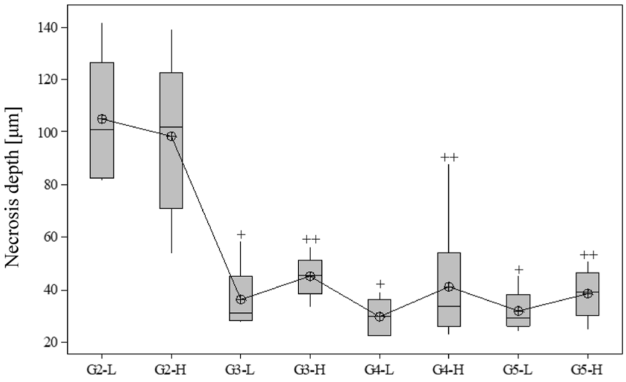

Fig. 11. Quantitative evaluation of thermal injury (necrosis depth) across experimental cases. (+: $P < 0.05$ vs. G2-L; ++: $P < 0.05$ vs. G2-H.).

clinical contexts[6,7]. Although the operating temperature of the proposed DUO blade was lower than that of the glass-coated devices, it exhibited a necrosis depth that was not statistically different from the glass-coated group. This phenomenon can be attributed to the DUO blade's intentional design, which allows a portion of the energy to be released through the lateral surface of the electrode to enhance hemostatic performance. This design characteristic is consistent with the hemostasis evaluation results presented later in this study. In contrast, glass-coated devices incorporate a thick glass layer along the lateral surface of the electrode, which serves as both an electrical insulator and a thermal barrier, resulting in a relatively high vertical temperature at the incision site but significantly reduced lateral heat transfer.

Blood loss

The method for evaluating blood loss at the incision site was designed with reference to the experimental procedure reported in a previous study[6]. Immediately after incision, a 110 mm diameter filter paper (Whatman Grade 6, Cytiva) was used to absorb blood for 60 s. As shown in Supplementary Fig. S5 and Table S3, the stained filter paper was then digitized using a flatbed scanner, and the discolored area was quantitatively analyzed using ImageJ software by measuring the number of stained pixels. The blood loss measurements presented in Fig. 12 confirm that the proposed DUO blade demonstrates excellent hemostatic performance, in line with its design objectives. As with the other box plots in this study, the box represents the range between the first and third quartiles, the horizontal line inside the box indicates the median value, and the whiskers show the entire range of data including the lowest and highest measurements. The average blood loss, measured in pixels, for each experimental condition was as follows: G1 (386,528), G2-L (1,515), G2-H (2,241), G3-L (11,743), G3-H (12,686), G4-L (72,965), G4-H (39,113), G5-L (14,122), and G5-H (21,343). Notably, its effectiveness was found to be comparable to that of conventional high-temperature electrodes, despite operating at significantly lower temperatures. Due to the small sample size ($n = 6$) and heterogeneous vascular distribution in the skin layers, normality assumptions were not fully met, which impacted the statistical significance of differences among certain groups. Nevertheless, it is noteworthy that the experimental group with a relatively thick glass coating (G4) exhibited markedly higher blood loss compared to the other groups, recording values 5.2 times and 1.8 times higher than those of the proposed DUO blade (G5) at 35 W and 50 W, respectively. This suggests that, in resistive heating-based systems, increasing the thickness of the lateral coating may help reduce operating temperature and thermal damage, but introduces a clear trade-off in terms of hemostatic performance. Ultimately, this implies that in conventional resistive heating-based electrosurgery, achieving lower incision temperatures often comes at the cost of reduced coagulation capability, particularly along the lateral surface of the electrode. These findings underscore the need for a fundamental shift in the energy delivery mechanism to enhance surgical safety without compromising performance.

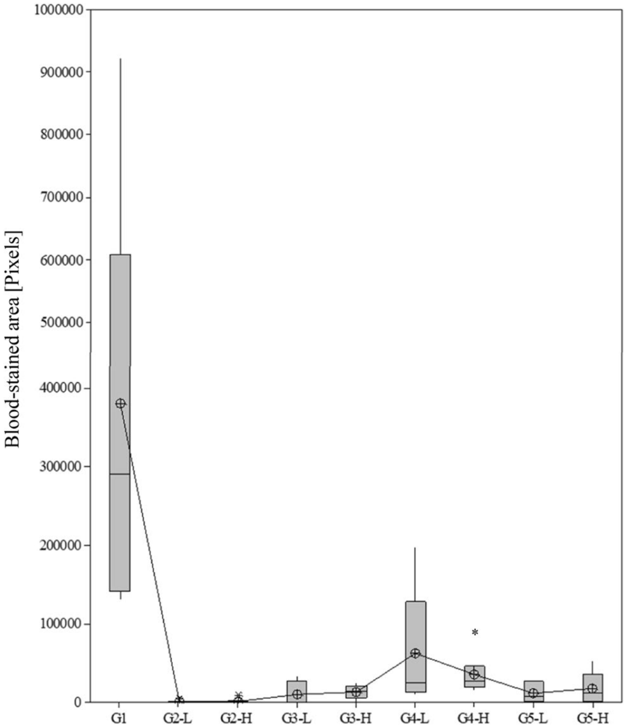

Fig. 12. Quantitative evaluation of blood loss per 3 cm of incision. (*: Outlier, defined as a data point exceeding 1.5 times the interquartile range (IQR) from the edge of the box.).

Surgical smoke

To quantitatively assess the microparticles contained in surgical smoke generated during incision, a light-scattering airborne particle counter (AeroTrak 9303, TSI) was employed. Based on previous studies reporting that microparticles generated during electrosurgery primarily range in size from 0.07 µm to 0.42 µm and occasionally reach several micrometers in diameter[16,17,45]this study focused on the quantification of particles measuring 0.3 µm and 0.5 µm in diameter. Considering that particles in the micrometer range are generally filterable by standard surgical masks[18]the analysis specifically targeted ultrafine particles that may pose greater health risks to medical personnel in real surgical environments.

To collect airborne particles, an air inlet with dimensions of 5 cm × 0.2 cm (1 cm^2) was placed 2 cm from the incision, and the inlet configuration and its position are illustrated in Supplementary Fig. S6. Air was drawn into an anti-static vinyl bag using a 400 LPM air pump. The connecting tube between the intake and the pump was selected to match the cross-sectional area of the inlet, ensuring consistent airflow. In order to minimize cross-contamination and ensure the independence of data across experimental groups, each case employed an independent configuration consisting of a separate air inlet, connecting tube, and air pump. Additionally, a sufficient ventilation period was introduced between experiments, and the next experimental case was initiated only when the laboratory air quality returned to within the pre-measured baseline range (G1). The air pump was synchronized with the start of the incision and operated for 3 s, corresponding to the duration of the cutting procedure. For each experimental case, the collected air was sealed in a single static-free vinyl bag. The inlet of the particle counter was then inserted into the sealed bag, and measurements were repeated 12 times to ensure consistency and statistical reliability.

The number of 0.3 µm and 0.5 µm particles counted under the aforementioned conditions is presented in Fig. 13(a) and (b), with the average values for each group provided in Supplementary Table S4. As with the previous box plots, the graphs indicate the minimum and maximum values, the median, and the first and third quartiles. The results related to surgical smoke exhibited a trend consistent with the findings from the previous temperature and tissue necrosis experiments, indicating that efforts to achieve lower operating temperatures lead to a reduction in surgical smoke. Both the G4 group, featuring a tapered geometry with a thick glass coating, and the newly proposed DUO blade, utilizing dielectric heating, exhibited statistically significant reductions in particulate generation compared to the conventional non-tapered, silicone-coated blade (G2) ($P < 0.05$). Among all experimental conditions, the DUO blade demonstrated the most substantial reduction in surgical smoke, decreasing the number of 0.3 µm and 0.5 µm particles by 31% and 27%, respectively, relative to G2. Compared to the tapered, glass-coated blade (G3), the DUO blade achieved additional reductions of 27% and 15% for 0.3 µm and 0.5 µm particles, respectively. Notably, while the DUO blade exhibited surgical smoke characteristics comparable to G4—the device with the lowest operating temperature among all resistive heating-based systems—it clearly outperformed G4 in hemostatic performance. Collectively, these findings validate the balanced and superior performance of the DUO blade, demonstrating that the dielectric heating mechanism can

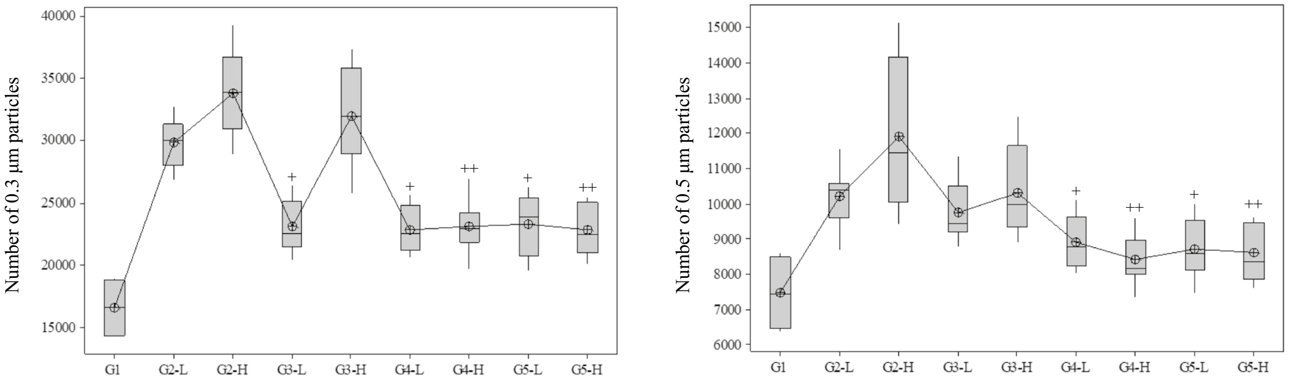

(a) The number of 0.3 µm particles in surgical smoke.

(b) The number of 0.5 µm particles in surgical smoke.

Fig. 13. Quantitative evaluation of surgical smoke across experimental cases. (+: $P < 0.05$ vs. G2-L; ++: $P < 0.05$ vs. G2-H.).

simultaneously enable low-temperature operation, effective coagulation, and significant reduction in surgical smoke—without requiring RF modulation or thick insulation layers.

Results

In this study, a novel Dielectric Ultra-Focused Oscillatory (DUO) blade was proposed, which utilizes a fundamentally different energy transfer mechanism—dielectric heating—as opposed to conventional resistive heating used in traditional electrosurgery. Designed to simultaneously achieve low-temperature cutting and effective hemostasis, the proposed DUO blade was optimized through finite element analysis (FEA) combined with machine learning, enabling precise control of the electric field distribution. The blade's unique geometry allows it to selectively heat intracellular moisture within tissue, leveraging the dielectric heating principle. This enables incision along the vertical axis while achieving coagulation along the lateral surfaces, as verified through both ex-vivo and in-vivo experiments. Experimental results confirmed that the DUO blade operates at significantly lower temperatures than conventional low-temperature electrosurgical devices, due to an inherent thermal cap of 100 °C imposed by the vaporization limit of water. This self-limiting temperature behavior led to significantly reduced tissue necrosis and surgical smoke production. Furthermore, the DUO blade effectively resolved the long-standing trade-off between operating temperature and hemostasis found in existing low-temperature electrosurgical technologies. The lateral electric field optimization contributed to improved coagulation without requiring elevated temperatures, confirming the efficacy of the proposed approach. Given its demonstrated advantages in low-temperature operation, minimal tissue necrosis, effective hemostasis, and reduced surgical smoke, the proposed DUO blade is expected to contribute to improved surgical outcomes for both healthcare professionals and patients, offering a well-balanced performance across these critical factors. Furthermore, as the DUO blade does not require specialized RF modulation or dedicated high-cost generators, it offers performance comparable to or exceeding that of conventional low-temperature electrosurgical solutions—at a lower system complexity and cost. These attributes suggest strong potential for reducing both industrial and societal healthcare costs. Several aspects are left for future work, including the analysis of cutting force across different generator output modes for the DUO blade, longitudinal tracking of post-incisional healing factors, precise monitoring of thermal and electrical parameters to maximize dielectric heating efficiency and enable generator-level control, and comparative evaluation against other advanced surgical energy modalities such as plasma, ultrasonic, and laser-based devices.

Data availability

All data generated or analyzed during this study are included in this article and its supplementary information file.

Received: 17 April 2025; Accepted: 17 July 2025

References

1. O'Cpnnor, J. L. Bloom. William T. Bovie and electrosurgery. *Surgery* **119**, 390–396 (1996).
2. Pethig, R. & Kell, D. B. The passive electrical properties of biological systems: their significance in physiology, biophysics and biotechnology. *Phys. Med. Boil.* **32**, 933–970 (1987).
3. Munro, M.G. Fundamentals of electrosurgery part I: principles of radiofrequency energy for surgery. In: Feldman, L., Fuchshuber, P., Jones, D. (eds) The SAGES Manual on the Fundamental Use of Surgical Energy (FUSE) 15–59. Springer, New York. (2012).
4. Brown, D. B. Concepts, considerations, and concerns on the cutting edge of raiofrequency ablation. *J. Vasc Interventional Radiol.* **16**, 597–613 (2005).
5. Massarweh, N. N. & Cosgriff, N. Slakey. Electrosurgery: history, principles, and current and future uses. *J. Amer Coll. Surg.* **202**, 520–530 (2006).

6. Loh, S. A., Carlson, G. A., Chang, E. I., Huang, E. & Palanker, D. Gurtner. Comparative healing of surgical incisions created by the PEAK plasmablade conventional electrosurgery, and scalpel. *Plast. Reconstr. Surg.* **124**, 1849–1859 (2009).
7. Messmer, D., Vose, J., Huang, E. & Kummel, A. C. Comparative healing of human cutaneous surgical incisions created by the PEAK plasmablade, conventional electrosurgery, and a standard scalpel. *Plast. Reconstr. Surg.* **128**, 104–111 (2011).
8. Schaller, R. D. A comparison of two insulated electrocautery blades: what is the thermal damage effect on transvenous cardiac device leads? *J. Innov. Card Rhythm Manag.* **9**, 3436–3438 (2018).
9. Wasserlauf, J. et al. Avoiding damage to transvenous leads – A comparison of electrocautery techniques and two insulated electrocautery blades. *Pacing Clin. Electrophysiol.* **41**, 1593–1599 (2018).
10. Memon, A. G., Naeem, Z. & Zaman, A. Zahid. Occupational health related concerns among surgeons. *Int. J. Health Sci.* **10**, 279–291 (2016).
11. Mowbray, N., Ansell, J., Warren, N. & Wall, P. Torkington. Is surgical smoke harmful to theater staff: a systematic review. *Surg. Endosc.* **27**, 3100–3107 (2013).
12. Kargalainen, M. et al. The characterization of surgical smoke from various tissues and its implications for occupational safety. *PLoS One.* **13**, 1-13 (2018).
13. Brandon, H. J. & Young, V. L. Characterization and removal of electrosurgical smoke. *Surg. Serv. Manag.* **3**, 14–16 (1997).
14. Ail, E. et al. Surgical smoke and infection control. *J. Hosp. Infect.* **62**, 1–5 (2006).
15. Wu, J. S., Luttmann, D. R. & Meiningerm, T. A. Soper. Production and systemic absorption of toxic byproducts of tissue combustion during laparoscopic surgery. *Surg. Endosc.* **11**, 1075–1079 (1997).
16. Swerdlow, B. N. Surgical smoke and the anesthesia provider. *J. Anesth.* **34**, 575–584 (2020).
17. Limchantra, I. V. & Fong, Y. Melstrom. Surgical smoke exposure in operating room personnel: a review. *JAMA Surg.* **154**, 960–967 (2019).
18. Bree, K. & Barnhill, S. Rundell. The dangers of electrosurgical smoke to operating room personnel: A review. *Workplace Health Saf.* **65**, 517–526 (2017).
19. Lee, S. & Grinshpun, S. A. Reponen. Respiratory performance offered by N95 respirators and surgical masks: human subject evaluation with NaCl aerosol representing bacterial and viral particle size range. *Ann. Occup. Hyg.* **52**, 177–185 (2008).
20. ASC Focus – Ambulatory Surgery Center Association. Three More States Adopt Surgical Smoke Evacuation Laws. (2024). https://www.ascfocus.org/ascfocus/content/articles-content/articles/2024/digital-debut/three-more-states-adopt-surgical-smoke-evacuation-laws
21. Medicines and Healthcare Product Regulatory Agency. Lasers, intense light source systems and LEDs – guidance for safe use in medical, surgical, dental and aesthetic practices. (2015). https://assets.publishing.service.gov.uk/media/5a75936f40f0b6360e475291/Laser_guidance_Oct_2015.pdf
22. The National Institute for Occupation Safety and Health. Control of smoke from laser/electric surgical procedures. (1996). https://www.cdc.gov/niosh/docs/hazardcontrol/hc11.html
23. Association of periOperative Registered Nurses. RI Governor Signs Smoke Evacuation Legislation. (2018). https://www.aorn.org/article/2019-09-27-RI-Governor-Signs-Smoke-Evacuation-Legislation.
24. Bennett, H. E. et al. Assessment of penetrating thermal tissue damage/spread associated with PhotonBlade™, Valleylab™ Pencil, Valleylab™ EDGE™ Coated Pencil, PlasmaBlade® 3.0S and PlasmaBlade® 4.0 for intraoperative tissue dissection using the fresh extirpated porcine muscle model. *in Proc. of SPIE*, 1–15 (2017).
25. Palanker, D. V. et al. Pulsed electron avalanche knife (PEAK) for intraocular surgery. *Invest. Ophthalmol. Vis. Sci.* **42**, 2673–2678 (2001).
26. Miller, J. M. et al. Precision and safety of the pulsed electron avalanche knife in vitreoretinal surgery. *Arch. Ophthalmol.* **121**, 871–877 (2003).
27. Palanker, D. V. et al. Electrosurgical system with uniformly enhanced electric field and minimal collateral damage. US Patent 7,736,361, (2008).
28. Borgmeir, P. R. et al. A review of capacitive return electrodes in electrosurgery. *J. Surg.* **9**, 31–35 (2021).
29. Nadolny, Z. Determination of dielectric losses in a power transformer. *Energies* **15**, 1–14 (2022).
30. Teri, D. D. et al. Dielectric properties of ex vivo Porcine liver tissue characterized at frequencies between 5 and 500 khz when heated at different rates. *IEEE Trans. Biomed. Eng.* **65**, 2560–2568 (2018).
31. Morris, M. L. & J. H. Hwang. Electrosurgery in therapeutic endoscopy. In: Vinay, C., Elmunzer, B., Khashab, M., Muthusamy, V. (eds) Clinical Gastrointestinal Endoscopy, 69–80. Elsevier. (2019).
32. Choi, B. H., Heo, J., Choi, I. & Lee, E. Dielectric ultra-focused oscillatory (DUO) monopolar blade for minimizing thermal damage in electrosurgical applications. presented at the *9th Int. Conf. Biomedical Engineering and applications*. (2025).
33. Choi, I. Conductive electrode for electrosurgical handpiece. U.S. Patent 20240115308, filed June 15, (2021).
34. Marguerat, S. Bahler. Coordinating genome expression with cell size. *Trends Genet.* **28**, 560–565 (2012).
35. Liangheng, L., Zhang, S., Ding, D. & Wang, Y. Path planning via an improved DQN-based learning policy. *IEEE Access.* **7**, 67319–67330 (2019).
36. D. Andreuccetti, R. Fossi and C. Petrucci., An internet resource for the calculation of the dielectric properties of body tissues in the frequency range 10 Hz - 100 GHz. *IFAC-CNR.* http://niremf.ifac.cnr.it/tissprop/ (1997).
37. Minih, V. et al. Human-level control through deep reinforcement learning. *Nature* **518**, 529–533 (2025).
38. Sutton, R. S. & Barto, A. G. *Reinforcement Learning: an Introduction* 2nd edn (Bradford Book, 2018).
39. Choi, B., Lee, E. & Kim, Y. Optimal structure design of ferromagnetic cores in wireless power transfer by reinforcement learning. *IEEE Access.* **8**, 179295–179306 (2020).
40. Jeong, M., Jang, J. & Lee, E. Optimal IPT core design for wireless electric vehicles by reinforcement learning. *IEEE Trans. Power Electron.* **38**, 13262–13272 (2023).
41. Gabriel, C., Gabriel, S. & Corthout, E. The dielectric properties of biological tissues: I. Literature survey. *Phys. Med. Biol.* **41**, 2231–2249 (1991).
42. Stoy, R. D., Foster, K. R. & Schwan, H. P. Dielectric properties of mammalian tissues from 0.1 to 100 mhz: a summary of recent data. *Phys. Med. Biol.* **27**, 501–513 (1982).
43. Valleylab Force FX^{TM}-C Electrosurgical Generator with Instant Response™ Technology. (2009). https://www.equippedmd.com/wp-content/uploads/2018/01/Valleylab-Force-FX-C-Operators-Guide.pdf
44. Medtronic Advanced Energy LLC. AEX™ Generator Operator's Manual. (2017). https://documents.cdn.ifixit.com/LdQaFgEjj2j34FqN.pdf
45. Casey, V. et al. Comparison of surgical smoke generated during electrosurgery with aerosolized particulates from ultrasonic and high-speed cutting. *Ann. Biomed. Eng.* **49**, 560–572 (2020).

Author contributions

Bo H. Choi conceived and designed the experiments, performed the experiments, analyzed and interpreted the data, prepared the figures, and wrote the manuscript. Jun H. Heo conducted the finite element method (FEM) simulations and performed the ex vivo experiments. Min S. Kim designed and executed the FEM simulations incorporating machine learning techniques. In S. Choi participated in the mechanical and material design of the electrodes and contributed to the in vivo experiments. Eun S. Lee contributed to the experimental design and FEM analysis, and reviewed and approved the final version of the manuscript.

Declarations

Competing interests

The authors declare no competing interests.

Additional information

Supplementary Information The online version contains supplementary material available at https://doi.org/10.1038/s41598-025-12578-3.

Correspondence and requests for materials should be addressed to E.S.L.

Reprints and permissions information is available at www.nature.com/reprints.

Publisher's note Springer Nature remains neutral with regard to jurisdictional claims in published maps and institutional affiliations.

Open Access This article is licensed under a Creative Commons Attribution-NonCommercial-NoDerivatives 4.0 International License, which permits any non-commercial use, sharing, distribution and reproduction in any medium or format, as long as you give appropriate credit to the original author(s) and the source, provide a link to the Creative Commons licence, and indicate if you modified the licensed material. You do not have permission under this licence to share adapted material derived from this article or parts of it. The images or other third party material in this article are included in the article's Creative Commons licence, unless indicated otherwise in a credit line to the material. If material is not included in the article's Creative Commons licence and your intended use is not permitted by statutory regulation or exceeds the permitted use, you will need to obtain permission directly from the copyright holder. To view a copy of this licence, visit http://creativecommons.org/licenses/by-nc-nd/4.0/.

© The Author(s) 2025